STARS

University of Central Florida
STARS

HIM 1990-2015

2013

Production, control and actuation of micron-sized particles in a microfluidic T-junction

James Wilson
University of Central Florida

 Part of the Mechanical Engineering Commons
Find similar works at: https://stars.library.ucf.edu/honorstheses1990-2015
University of Central Florida Libraries http://library.ucf.edu

This Open Access is brought to you for free and open access by STARS. It has been accepted for inclusion in HIM 1990-2015 by an authorized administrator of STARS. For more information, please contact STARS@ucf.edu.

Recommended Citation

Wilson, James, "Production, control and actuation of micron-sized particles in a microfluidic T-junction" (2013). *HIM 1990-2015*. 1484.
https://stars.library.ucf.edu/honorstheses1990-2015/1484

PRODUCTION, CONTROL AND ACTUATION OF MICRON-SIZED PARTICLES IN A MICROFLUIDIC T-JUNCTION

by

JAMES WILSON

An Honors Thesis submitted in partial fulfilment of the requirements
for the degree of Bachelors of Science in Mechanical Engineering with Honors
in the College of Engineering and Computer Science
at the University of Central Florida

Spring Term 2013

Thesis Chair: Ranganathan Kumar

© 2013 James Wilson

ABSTRACT

This research is directed towards understanding the mechanisms associated with the manufacture of solid microspheres less than $100\mu m$, from liquid droplets with nanosuspensions in a microfluidic T-junction, which are heated downstream of the channel. Preliminary material characterization tests on colloidal suspensions of alumina and copper oxide demonstrate promising temperature dependent viscosity results indicating solidification in the temperature range of 40^oC-50^oC. The solidification mechanism is referred to as Temperature Induced Forming and is described by polymeric bridges formed between nanoparticles in suspension at elevated temperatures, resulting in a solid structure. The polymer network results from the ionization of alumina at elevated temperatures whereby polymeric binders adhere to newly formed charged sites on the alumina particle. This study aims to investigate the aspects of manufacturing microstructures in microfluidic T-junctions, droplet morphology, size and frequency of production. Preliminary low solid concentration experiments (1%-10% volume concentration of alumina in H_2O) have indicated solidification and a regression in droplet diameter when heated near the saturation temperature of the water used to disperse the particles. The microstructures formed in the microfluidic device by this solidification process are uniform and are estimated to be $30\mu m$ in size.

DEDICATION

This thesis is dedicated to my loving family and those who have encouraged me to go further and achieve more. To my advisor Ranganathan Kumar for guiding me along the way and my colleague and friend Jonathan Wehking for equipping me with the tools and perspective to become a stronger, more capable individual.

TABLE OF CONTENTS

LIST OF FIGURES

LIST OF TABLES

CHAPTER 1: INTRODUCTION/LITERATURE REVIEW

For the past decade, Microfluidic devices (MFDs) have been used in several applications such as droplet generation, mixing of chemical reagents, bacterial isolation and solid formation. Thorsen *et al.* [1] achieved the production of monodisperse droplets in a cross flow microfluidic device (T-junction) and since, there have been several developments in this area of study. Conceptually, a T-junction consists of a T-shaped geometry of intersecting channels where an immiscible fluid pair intersect; the discontinuous fluid would emerge in the continuous flow and a combination of forces would cause the discontinuous flow structure to destabilize and break-up resulting in droplets or plugs within the continuous stream. Figure 1.1 illustrates the cross flowing MFD T-junction geometry utilized for the production of monodisperse droplets in the current study.

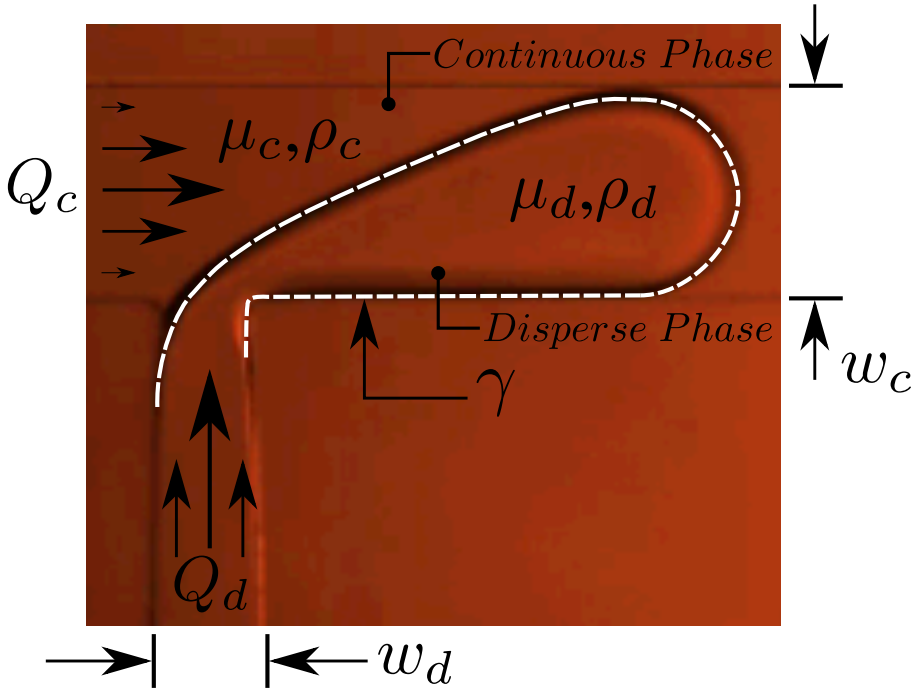

Figure 1.1: T-junction and defining characteristics

The subscripts c and d denote the continuous and dispersed flows respectively, Q denotes the volumetric flow rate, w denotes the channel width, γ denotes the interfacial surface tension (dashed white line) and the material properties μ and ρ are the viscosities and densities, respectively for the continuous and dispersed fluids. The formation of droplets, as suggested above, is the result of flow destabilization and break-up. This was initially proposed to be a consequence of shear forces imposed on the discontinuous flow by the continuous flow [1] and later pressure forces at low continuous flow rates [2]. There arises a balance between stabilizing surface tension forces and destabilizing shear and pressure forces imposed on the discontinuous fluid that cause breakup in a microfluidic T-junction. The dynamics associated with droplet break-up has been discussed extensively in [3–11]. These papers developed parametric correlations relating flow conditions, material properties and geometric aspects to droplet formation characteristics such as size and frequency of production for various flow regimes (such as squeezing, dripping etc.) . The following section identifies correlations and studies related to production of monodisperse droplets in MFDs

Microfluidic Flows

Microfluidic flows are characterized by sufficiently small Reynolds numbers ($Re = \rho U l/\mu$ where ρ, U, l and μ are the fluid density, speed, characteristic length and dynamic viscosity respectively) where inertial forces become negligible and flow characteristics are determined by pressure gradients and viscous effects. For these sufficiently small Reynolds numbers ($Re << 1$) in the case of cross flowing geometries such as those utilized in this study, Capillary forces ($Ca = \mu_c U_c/\gamma$ where μ_c and U_c are the dynamic viscosity and speed of the continuous fluid as defined in the previous section and γ is the iterfacial surface tension between the fluid pair) govern the regimes and flow patterns observed within the MFD.

Squeezing and Dripping Regimes

Generation of monodisperse droplets within an MFD requires the understanding of forces involved between the continuous and dispersed flows. Research in the field of microfluidic droplet production [3–11] has provided a means of predicting droplet size and even morphology through geometric confinement.

Microfluidic flow regimes can be characterized primarily by the Capillary number; the two most notable regimes are distinguished by the presence of shear forces acting on the fluid/fluid interface of the fluid pair. For sufficiently low Capillary numbers ($Ca < 10^{-2}$) break up at the T-junction is a result of pressure drop across the fluid/fluid interface and restoring surface tension forces. Here, shear forces that would otherwise deform the emerging droplet are negligible and the discontinuous flow is allowed to emerge fully into the continuous channel temporarily blocking the continuous flow. As the dispersed fluid continues to flow while confined by the opposing wall of the device, the slug begins to grow and elongate until the upstream pressure forces are sufficient to cause neck formation at the T-junction and eventually detachment. This is referred to as the *squeezing* regime and is characterized by low Capillary numbers. For increasing Capillary numbers, the mechanisims associated with break-up shift from pressure to viscous shear forces described by Thorsen *et al.* [1]. This regime is referred to as the *dripping* regime and is characterized further by the location of droplet detachment from the upstream discontinuous flow [12]. Thus, the dripping regime could exist either at the junction or at the end of a fluid thread forming away from the junction. Droplet breakup for Capillary numbers beyond the critical Capillary number ($Ca > .015$) , as defined by De Menech *et al.* [12] falls within the *dripping* regime where further increasing the Capillary number results in a flow structure referred to as the *jetting* regime as suggested above where the discontinuous flow forms a parallel flow type thread where flow instabilities induce the formation of a neck and ultimately break-up.

Garstecki *et al.* [2] present a scaling relation describing the normailzed length of a slug, or simply a droplet experiencing confinement (l/w_c where l and w_c are the droplet lengths and the continuous channel widths respectively). The correlation suggests independence of the droplet length from the Capillary number and a large dependence of rates of flow. The authors varied the Capillary number by two orders of magnitude and the continuous fluid viscosity by a single order of magnitude. The normalized droplet length plotted against the flow rate ratio indicated consistency and independence of droplet size from the Capillary number and even the viscosity ratio for low Capillary numbers.

Objectives

A novel approach to the production of solid particles through Temperature Induced Forming (TIF) of nanoparticles suspended in droplets generated in a T-Junction will be presented in this work. Most of the mechanisms that induce solidification have been the result of chemical reactions, polymerization and self assembly; however, no mention has been made to specific fluids subject to solidification. Nanoparticle suspensions are of particular interest as their composition can result in a functional droplet with a wide range of properties [13, 14]. The specific objectives are given below.

• Develop a method of determining interfacial tension of dispersed and continuous fluid pairs and report value.

• Determine the rheological properties of alumina suspension at various concentrations and across a range of temperatures.

• Utilize a T-junction microchannel and apply the previously determined parameters to produce monodisperse droplets containing alumina nanosuspensions.

• Produce microspheres through Temperature Induced Forming by heating the Microfluidic T-junction for collection and observation to determine the solids diameter.

Applications of MFDs from Literature Search

Studies in MFDs have focused on geometric and material parameters of the microfluidic T-junction such as the ratio of continuous channel to disperse channel widths, $\Lambda = w_d/w_c$, viscosity ratio, $\lambda = \mu_d/\mu_c$ and the channel height to the continuous channel width ratio, $\Gamma = h/w_c$ [15–17]. These studies in the field of experimental and theoretical microfluidics have outlined the effects of common geometric and fluid properties making the design of a MFD easier to predictably produce monodisperse droplets and plugs. The following section identifies common applications in microfluidic devices such as medical and even manufacturing of solids from specific flow structures.

Due to the control over placement of fluid flows and intricacy of possible designs, MFD have become particularly popular in the science and research industry. These devices can eliminate the need for larger testing facilities and materials required for experimentation. MFDs have made a great impact on the medical industry by providing control over conditions such as fluid flow and geometry in order to mimic patterns found in the human body that were previously difficult to achieve in conventional culture dishes. Cell isolation can be achieved through the use MFDs where bacterial cultures can be observed, incubated, treated etc, in a controlable environment with repeatability.

Solid Production

Applications for these microfluidic geometries span a spectrum of industries ranging from medical and pharmaceutical to manufacturing [18–23]. Kenis *et al.* showed that microfluidic devices could be used to produce wire by merging electro-less silver plating solutions in another common geometric configuration referred to as a Y-junction, resulting in a thin sheet of silver. Control over the resolution of the features of such a product was proposed to be within $5\mu m$ and control over spatial location within $5\mu m$.

Solid production within MFDs typically results from chemical interactions at fluid/fluid interfaces or within either the dispersed phase, continuous phase or any combination of phases utilized in the experiment. The mechanisms for solidification can be a result of the aforementioned fluid/fluid interfacial chemistry, a time delayed solidification reaction within one of the phases or by an external influence to induce solidification by passage through a section of the MFD (reaction said to take place *in situ*) or beyond the domain in some sort of reactor (reaction said to take place *ex situ*).

Reactions taking place at the interface can be used to produce structures similar to those produced by Kenis *et al.* [23]; however, this type of interfacial reaction does not necessarily have to be fixed in space relative to the device at the fluid/fluid interface. The solidification can take place via droplet interfacial reactions with the continuous medium where the resulting solid structure would be free to flow through the domain. Reactions fixed in space require the disassembly of the device in order to harvest the product, as was the case for Kenis *et al.* due to the nature of the geometric confinement. This type of solid assembly process, though innovative, is unconventional with regard to scaling and increasing the rate of production as the product collection requires disassembly, harvesting, reassembly, and flow stabilization time which not only introduces the possibility of contamination and undesired chemical reaction, but costs associated with the time required for the downtime procedures. A more realizable product such as spheres, sphereoids or

plugs can be produced in common MFDs such as the T-junction. In this scenario, dispersed phase would then be allowed to travel through the MFD and react with the continuous fluid. The solid would then exit for collection permitting the device geometry is large enough to accommodate the largest characteristic dimension of the solid.

As discussed above, the state of microfluidics and their applications in producing solids is still at an infant stage. Christopher *et al.* [3] reviewed the field of microfluidics and the use of various geometries developed to produce a variety of flow structures and operational regimes (Squeezing, Dripping, DTJ, DC, PF etc.) [3]. This work summarized the state of particle production in various geometries and with various fluid pairs. The information presented also described the manner in which the dispersed phase was solidified; the solidification mechanisms presented were photo-polymerization via UV exposure *in/ex situ*, thermal-polymerization via batch heating *ex situ*, etc. Among these solidification techniques, the use of the geometry and flow parameters were identified as a means to tailor specifically shaped discontinuous flow structures (morphology), e.g. continuous tubes or droplets of specific size and shape etc. Another more comprehensive review specific towards particle production, [24], had been conducted prior to Christopher *et al.* [3]. The following section will describe some of the more distinctive developments in the field of particle generation in MFDs.

Photo Polymerization

Studies conducted [13, 14, 25–36] show that photo catalytic manipulation both *in situ* and *ex situ* of the discontinuous fluid can be utilized to preserve the morphology of the discontinuous flow. Target morphologies such as tubes, plugs, disks and even two phase *Janus* particles were demonstrated through geometric confinement and the use of flow focusing geometries [14, 26, 32–34, 37]. Photo polymerization relies on the use of external UV light sources incident on the MFD or on

an external batch of droplets produced in a MFD to induce solidification. Dendukuri *et al.* [34] utilized *in situ* photo polymerization to produce droplets of precise size and morphology through geometric confinement. Jeong *et al.* [26] demonstrated the formation of polymeric micro-fibers and micro-tubes consisting of 4-hydroxybutyl acrylate via *in situ* photo-polymerization of flow structures formed by coaxial MFD geometries. Paquet *et al.* [13] demonstrated the production of super-magnetic microspheres with tunable porosity. The group used an alternating copolymer of polystyrene and poly maleicanhydride and polyvinyl alcohol as a photo initiator and the Super-paramagnetic iron oxide nanoparticles (SPIONs) with fatty acids ligands as the dispersed particle phase which produced the desired functional effects.

Thermal Polymerization

Thermal polymerization occurring *ex situ* [36–39] is another means by which the discontinuous droplets can be solidified. Pioneering work in the field of particle production in a MFD conducted by Sugiura *et al.* [25] utilized a microfluidic emulsification technique to produce monodisperse hydrogenated fish oil spheres (melting temperature 58^oC) through the cooling of the preheated disperse fluid within the MFD. Nisisako *et al.* [36] produced spherical droplets composed of isobornyl acrylate and DAROCUR 1173 (Photo-initiator) referred to as beads which were collected and solidified via photo and thermal polymerization *ex situ*. Multiple techniques have been utilized to maipulate the temperature of the fluids within the MFD. Processes outlined by Siegel *et al.* [40] provide a means by which liquid solder can be sucked through a blank channel within PDMS. The process is referred to as microsolidics and utilizes the surface chemistry of the PDM after oxygen plasma treatment to allow for manipulation favoring the wetting of indium solder. The resulting solid indium channel canbe then utilized to generate heat through Joule heating. Other techniques require simply the heating of the continuous or dispersed fluid in order to induce solidification [41]. More advanced techniques utilize focused light beams whereby the optical properties of metallic

nanostructures become an efficient means for the conversion of light energy to heat [42]. Fang *et al.* [43] presented a method by which gold nanocrystals are distributed throughout PDMS forming a plasmonic composite enabling plasmon-enabled photothermal conversion, the same fundamental process presented by Cao *et al.* [42].

Organic Binders

In the Biomedical field the use of agarose and other polymeric thermal setting binders have been utilized to isolate bacterial cultures and contain reactions as droplets composed of immiscible fluids inhibit the diffusion of species across boundaries. Eun *et al.* [44] utilized agarose to contain E. coli using Fluorescence Activated Cell Sorting (FACS) via *in situ* thermal gelation. More recently, Sungmin *et al.* [41] utilized *in situ* thermally induced assembly of collagen fibers within the disperse phase encapsulating cells. This work demonstrates a novel method by which cell containing microspheres could be produced with an increase in cell viability and reduction in droplet coalescence through innovative collection procedures. The report also identified other commonly used biodegradable polymers used for the encapsulation of live cells such as alginate and polyethylene glycol (PEG). The use of these materials promotes the transport of nutrients and oxygen due to their porous nature, promoting the viability of the encapsulated cell [45].

Evaporation Induced Self Assembly

Studies conducted [46, 47] have presented the formation of nanoparticle clusters where the continuous and dispersed phases are miscible. In these cases, fluid miscibility results in what is referred to as Evaporation Induced Self Assembly (EISA) whereby particles in suspension assemble at the liquid/liquid interface forming a shell due to the diffusion of their suspending medium into the surrounding carrier fluid. Due to the low concentration of nanoparticles in suspension, the

structure formed was hollow. Another parameter referred to as the local Peclet number, P_e, a non-dimensional number quantifying evaporation effects relative to particle diffusion within the droplet, was correlated with morphological transitions from a spherical hollow structure to bowl and ring shaped structures. These shapes formed as a consequence of high P_e ($P_e >> 1$) and hence, rapid diffusion of the droplets suspending fluid into the surrounding continuous medium resulting in the buckling of the shell formed due to the inability of the nanoparticles to rearrange at the interface. The resulting asymmetry was proposed to be a consequence of the ratio of initial droplet diameter to the channel height [47].

Solid Formation from Colloidal Suspensions

Temperature Induced Forming

Nanosuspensions such as alumina and copper oxide and their stability characteristics are governed by a complex set of molecular interactions influenced by Brownian motion, van der Waals attractive forces, Electrostatic Double Layer (EDL) repulsion, steric repulsion etc. where the sum of these forces determines the nature in which the particles remain suspended in solution. This technique for determining the net attraction is referred to as the Derjaguin and Landau, Verwey and Overbeek (DLVO) theory and has become a standard when considering the stability of a colloid. It will be shown that the manipulation of temperature results in a great deal of changes in particle interaction and as a result, the rheology of the colloid, e.g. alumina and CuO suspended in H_2O with surfactant. The increase in temperature of these colloidal stable suspensions tends towards polymeric inter-particle bridging resulting in a state of irreversible flocculation (agglomeration) referred to as Temperature Induced Forming (TIF) [48]. The following sections describe the fundamentals of colloidal stability and standard ceramic forming methods in order to bridge the gap between TIF in ceramic processing and its novel application in MFDs.

Ceramic Forming Processes and Colloidal Stability

Colloids, also referred to as an emulsion in which the smallest length scale is $< 1\mu m$, have applications in many industries including ceramics and manufacturing. Colloids consisting of clay powders with high solid loadings (solid content relative to other constituents) such as silicon carbide (SiC) and alumina can be utilized to produce rock-hard solids simply by pouring into a prefabricated mold, drying, and sintering (heating), resulting in a solid body with valuable properties such as low weight, wear resistance, thermal insulation and resistance to corrosion. The resulting solid body is known as a ceramic and has become an essential engineering material due to the unique combination of properties described above. A typical method used in the manufacture of ceramics is known as injection molding; the process begins with a ceramic slip (suspension of ceramic particles) of desired composition and component concentrations, and is then injected into a mold shaped like the desired form of the final part, i.e. in a near net shape. The ceramic slip, or slurry, is then left to dry to form what is referred to as a green body which is firm enough for handling but still brittle. The dried parts complete their basic manufacturing stage through a process known as sintering where the green body undergoes atomic restructuring as a result of elevated temperatures, where it becomes a solid ceramic body.

There exist many methods by which solid green bodies can be produced while satisfying the economical requirements of near net shape forming techniques. The simple process of casting the part and allowing adequate time to dry results in parts of uniform properties and high reliability and mechanical strength; however, on a manufacturing scale this process is costly as drying times required to produce a solid green body dry enough to support its own weight without deformation require that it stay in the mold to retain its shape while drying. This drying time is dependent on part size and environmental conditions, lending to extensive variability in drying times and hence downtimes as molds are occupied by drying parts.

Lange *et al.* [49] explored the shortcomings of existing ceramic processing methods and proposed a more scientific approach for developing more efficient techniques through the understanding of colloidal science. This paper marked the development of what would become a rapidly developing field of colloidal ceramics processing in an effort to optimize the methods for the production of ceramic green bodies.

Colloidal suspensions and their stability require a balance of inter-particle forces. Not only do these forces determine stability but also the rheological behavior of the resulting suspension. Brownian motion acts to disperse the particles where attractive van der Waals forces tend towards particle agglomeration and the formation of flocs, or simply clusters of particles. Control over stability is possible through the manipulation of EDL forces and steric repulsive forces. Electrostatic forces occur as the particles submerged in a suspending medium possess a surface charge, especially when the intervening medium is polar, such as water; the surface charges can be manipulated by adjusting the pH of the solution or by the addition of ionic surfactants, thereby increasing the magnitude of similar inter-particle charges, increasing inter-particle repulsion, promoting colloidal stability. Steric repulsive forces are attributed to the presence of surfactants and the increasing physical separation between dispersed droplets/particles due to the surfactant assembly at the interfaces. The surfactants considered here and commonly in the colloidal sciences are amphiphilic in nature, meaning they possess hydrophobic and hydrophilic properties at opposite ends of the molecule, i.e. the molecule possesses heads of opposite polarity. This artifact contributes to understanding that surfactants assemble at phase interfaces as the respective sites on the surfactant molecule associate with the medium in which it is soluble. The self-assembly at the interface acts to decrease the free surface energy and hence, influences the interfacial characteristics of the colloid or emulsion, and in this case, acts to promote colloidal stability through physical separation and mitigation of van der Waals attractive forces.

Ceramics processing techniques through the use of colloidal suspensions have proven to be an effi-

cient means by which green bodies can be produced in a near net shape; however, one fundamental obstacle continues to be the drying time associated with the formation of these ceramic green bodies. Equipped with the knowledge of colloidal stability, one could produce a ceramic green body simply by manipulating the parameters associated with colloidal stability to induce flocculation, and hence, eliminating the down time required for the drying of the slip in the cast or mold; as a result, these techniques increases efficiency and reduce costs associated with the practical limitations above. The following section will introduce near net shape forming techniques that utilize colloidal de-stabilization to induce flocculation of a ceramic slip to form a green body. The details of the chemical reactions will be omitted as they are beyond the scope of this study; however, a conceptual overview of three typical forming processes and their consequences on the resulting green body will be discussed.

Temperature Induced Gelation

TIG is a reversible process in which a sterically stabilized suspension using an amphiphilic polymer (possessing both hydrophobic and hydrophilic properties) in pentanol is reduced in temperature ($\sim 20^oC$) whereby the solvency of the polymer in pentanol decreases with temperature; the result is a collapse in the polymer layer separating the particles and consequently a van der Waal force dominated flocculated state for the suspension [48].

Direct Coagulation Casting

DCC is utilized by an electrostatically stabilized suspension (pH or salt content modification) where the mechanism of flocculation is a result of two factors; a reaction or urea producing ammonia which increases the pH of the solution to its iso-electric point (IEP) where the zeta potential is zero and the increase in ionic strength through the formulation of ammonium bicarbonate and

ammonium carbonate compressing the EDL [50].

Application in MFDs

Among the techniques implemented to induce solidification in a microfluidic device, the colloidal forming techniques described above have potential to be implemented in existing MFDs. The physics governing the solidification would, in theory, still apply. The only difference would be the manner by which the un-solidified body is formed. Injection molding and casting would be replaced by the dispersion of droplets or tubes within the MFD. The feasibility of formation methods and use in an MFD would be determined by the fluid pairs utilized and their compatibility with the physics associated with droplet breakup. Few foreseeable obstacles stand to inhibit such applications. Direct Coagulation Casting (DCC) takes place over a time scale on the order of minutes up to hours, determined by the composition of the slurry to be de-stabilized. The use of this method in a MFD would require adequate time to solidify as to prevent coalescence; permitting of course the confinement of the droplet surrounded by an immiscible fluid does not retard the coagulation of the particles in suspension. Temperature Induced Gelation (TIG) too would require cooling and heating *in situ* respectively to prevent coalescence and complete formation of a solid particle. The solidification methods presented at the beginning of this report act as templates by which the ceramic formation techniques could be implemented, particularly the sources that utilize agarose (solidification upon cooling corresponding to TIG) or those utilizing thermal polymerization (solidification upon heating corresponding to TIF).

Colloidal processing methodologies have been developed and optimized for use in ceramic manufacturing industries; however, as proposed above, they are not limited to existing manufacturing techniques (injection molding, casting, etc.) but are applicable wherever the necessary catalysts are available (thermal, chemical, etc.).

Solid Particles in a MFD

The aforementioned methods for producing solid particles in MFDs drive an interest to produce monodisperse droplets of chosen size and morphology via TIF in a T-junction. Droplets with high solid loading can be solidified, and sintered, resulting in highly uniform near net shape ceramic microspheres with applications as paint additives lending to low reflectivity and high durability coatings, as additives to aerosol paints to promote reflection (silica), as tuning and calibration tools, e.g. as spacers due to mobility and mono-dispersity and as calibration tools for sieves. Microspheres can also be used for micro-PIV, density determination of variable density fluids and even in marine biology through simulation of roe dispersion through the dispersion of comparable size and density spheres. The following sections outline practical concerns associated with the use of high solid loading suspensions in a MFD and the consequences affecting the TIF process by mitigating these limitations.

Limitations of High Solid Loading Suspensions

Preliminary results have shown that it is indeed possible to produce monodisperse particles through TIF; however, in order to effectively control the physics associated with break-up at the T-junction, the aqueous nanoparticle suspensions utilized were reduced in concentration in order to lower viscosity. By diluting a stock concentration of a 12.7% volume concentration of an aqueous suspension of CuO to 6.3%, viscosity decreased from $\sim 400cP$ to $5cP$. The resulting viscosity of the dispersed phase makes manipulation of the resulting droplets more achievable and mitigates non-Newtonian behavior inherent in high solid loading aqueous nanoparticle suspensions. A consequence resulting from reductions in solid loadings of these aqueous suspensions is a reduction in the active number of positively charged adhesion sites that form during ionization, Figure 3.3, to which the surfactant can bond in order to form an inter-particle network; consequently, this reduces

the stability of the resulting solid particle. Low concentrations of solids and even surfactants used for temperature induced inter-particle bridging have shown that there exists a relation between the gelation temperature and concentration of components in suspension [51]. Yang *et al.* [51] also noted that for aqueous suspensions of alumina, solid loadings below the gelation threshold (minimum volume fraction of solids below which gelation will not occur for a given shear rate, type and concentration of surfactant), the bridges forming between particles are destroyed due to shearing of the moving fluid during measurement in the viscometer, as a result, no appreciable increase in viscosity was observed.

These artifacts suggest the existence of an optimal nanoparticle concentration range for use in a MFD. Below such a range, solidification will not occur where the destruction of weak inter-particle bridges could be attributed to the forces associated with droplet coalescence, similar to the previously noted shear force imposed by the measurement tool. Above this range, practical limitations such as the viscosity of the dispersed phase flowing through the MFD may retard the effective production of small scale droplets at the T-junction or even clog the downstream section of the MFD.

CHAPTER 2: METHODOLOGY

In two-phase microfluidics, emphasis on sample quality and material characteristics must be applied cautiously as sample sizes are relatively small when compared to the contact surface area of the surroundings. Significant variations in interfacial tension for water dispersed in air have been observed by utilizing syringes out of the package. Reported data should reflect the conditions utilized in the experiment, therefore, the interfacial tension and viscosity values reported and utilized in analysis should be those values resulting from material characterization designed to reproduce the conditions of the experiment.

Material Characterization

The study reported in this thesis requires the knowledge of fluid properties such as viscosity, density and fluid pair interfacial surface tension. Many methods exist for characterizing the aforementioned; however, most of the values are available from the fluid manufacturer or are common knowledge and found in the literature. In the case of proprietary fluid mixtures, such as those utilized in this study, a thorough material characterization study must be conducted in order to complete analysis and even predict an outcome when designing an experiment. The following sections outline the procedures for identifying material properties for use in MFD experimentation.

Viscosity

Fluid viscosity, or a fluids ability to resist shear deformation in 2-D is described by the equation $\tau = \mu \frac{\partial u}{\partial y}$. Where τ is the shear stress at a point separating fluid layers and μ is a constant of proportionality relating the shear stress to the change in speed of the fluid layers , Δu, over the rate

of change across layers, Δy. This constant of proportionality is the dynamic viscosity with units of $Pa * s$.

In house methods for determining and validating fluid viscosity were implemented by utilizing the Brookfield DV II+ PRO viscometer with ultra low sample adapter (UL Adapter). The device measures viscosity by turning spindle inside of a concentric cylinder designed to contain the fluid. The geometric configuration of the spindle in outer cylinder can be seen in Figure 2.1.

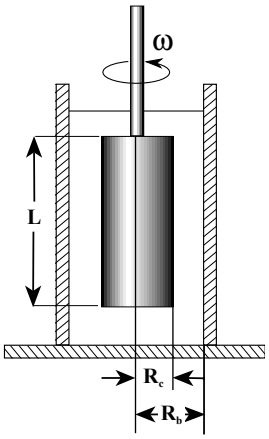

Figure 2.1: Schematic of Brookfield UL Adapter for measuring viscosity

The drive mechanism connects to the inner cylinder and supports the pull of gravity; however, the added torsion caused by the shearing fluid is transmitted through the cylinder to a spring. It is the springs rotational deflection paired with other characteristic geometric and operational parameters that are utilized to determine the viscosity of the fluid which is contained by the outer cylinder. The stiffness of this spring was selected by the manufacturer such that light weight fluids, such as water and oils (1-100cSt) will lead to a deflection ideal for the measurement of torque. The device is pre-programmed with a database of available spindles/spindle-adapter sets ranging from $S00$-$S99$ (UL Adapter: $S00$). These spindles and their associated geometries contribute to an analytical expression for the viscosity in terms of the shear rate $(\dot{\gamma})$, shear stress (τ) and finally the viscosity (μ). Equation 2.1 outlines how the parameters above can be calculated through geometric and

measurable parameters (torque from spring deflection).

$$\begin{aligned} \dot{\gamma} &= \frac{2\omega R_c^2 R_b^2}{x^2(R_c^2 - R_b^2)} \\ \tau &= \frac{M}{2\pi R_b^2 L} \\ \mu &= \frac{\tau}{\dot{\gamma}} \end{aligned} \tag{2.1}$$

where x is the distance in the fluid where the shear rate is estimated, ω is the rotational speed in $\frac{rad}{s}$ and M is the torque measured internally by the deflection of the spring.

Operation of the viscometer is made simple by the use of the built in range features as well as simplified control of the rotational speed. The viscometer configuration is conducive to measuring the temperature dependence of the sampled fluid as the thin stainless steel wall of the UL Adapter allows for the conduction of heat into the sample fluid. Simulations of steady state temperature distributions within the UL Adapter of Alumina have demonstrated radial and height variations in sample temperature on the order of 1^oC and for a constant external surface temperature, verifying the feasibility of accurate temperature measurements. The UL Adapter was submerged into a heated and continuously mixed water bath to promote uniform temperature on the outer surface of the UL Adapter. Temperature values of the bath were recorded along with the output viscosity values from the viscometer. Verification of this method was conducted by comparison of experimental results with manufacturers specifications and can be seen in Figure 2.2.

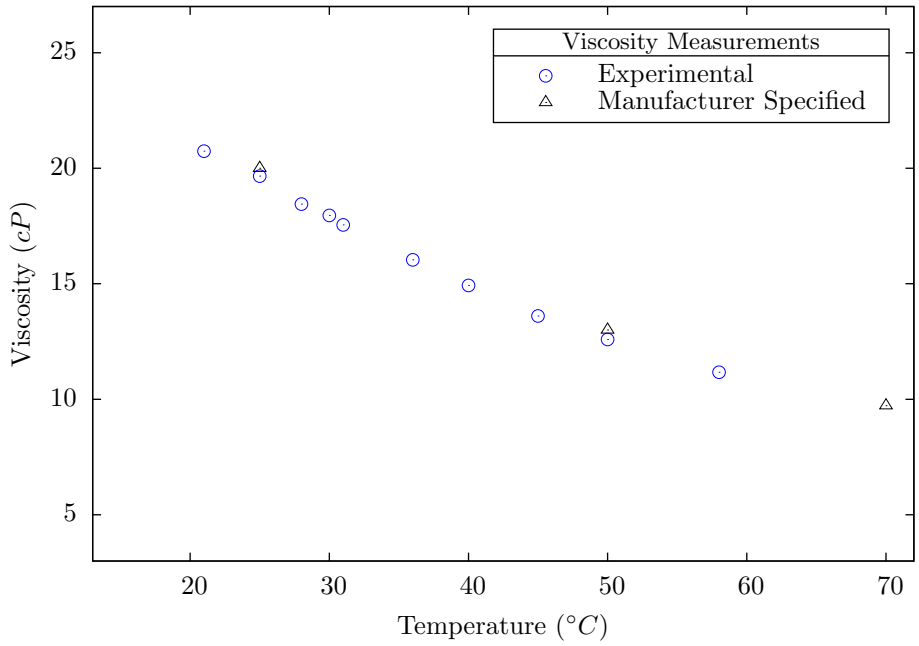

Figure 2.2: Verification of $20cSt$ PDMS Oil viscosity measurements using heated water path

Viscosity Measurement Obstacles

Increasing the speed of the viscometer, ω, decreases the time required for viscosity output to stabilize; however, by increasing the speed, due to the limitation of the torsional spring, the upper range of measurable viscosity decreases as the shear rate scales proportionally with the shear stress through the fixed viscosity. Also, speed variation is a concern when considering non-Newtonian fluids as the measured viscosity is dependent on the measurement speed. In the case of this study, $20nm$ Alumina dispersed in H_2O exhibits non-Newtonian behavior as demonstrated in Figure 2.3. The characterization of aluminas viscosity dependence becomes problematic as Alumina can solidify due to TIF, beyond the measurable range of the viscometer for the fixed speed. As a result, speed must decrease as the Alumina viscosity approaches the upper viscosity limit. Since the non-Newtonian behavior is less significant, the viscosity of Alumina is accepted with slight error

after the rotational speed is decreased due to the increasing viscosity. The viscosity data for the temperature dependence of Alumina will be discussed later in Chapter 3.

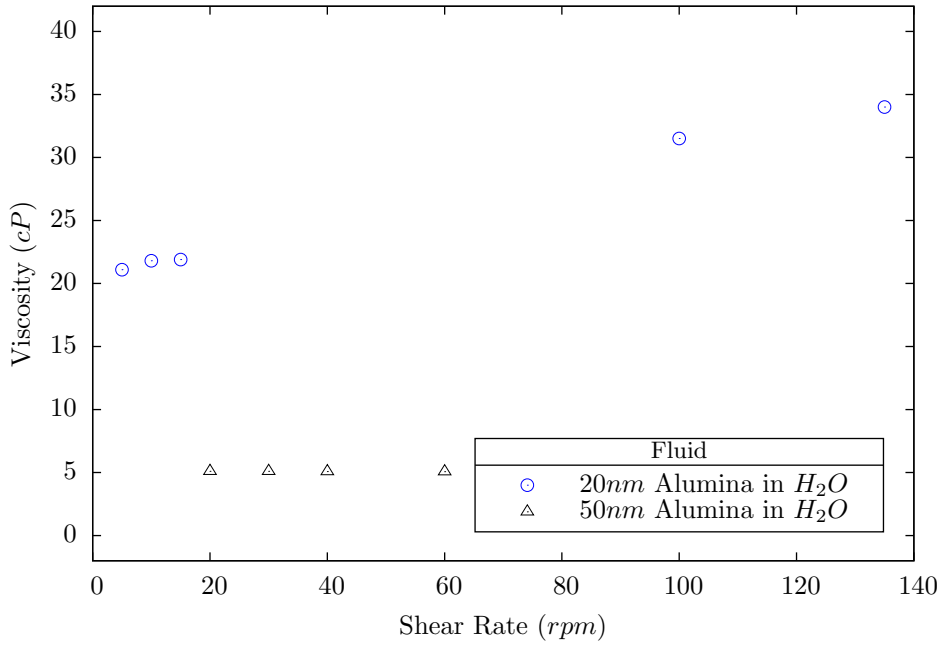

Figure 2.3: Characterization of non-Newtonian behavior of Alumina dispersed in H_2O with dispersant

Interfacial Tension

Interfacial tension is a measure of the force imposed at a fluid-fluid interface due to molecular interactions and the transition from one bulk fluid phase to another. This force is dependent on the fluid pair and the additives or particlessuspended in the medium. An example of interfacial tension is the ability for a droplet of water to remain attached to a leaky faucet or how a drop of water forms a bead on a freshly waxed car. In the case of the water droplet hanging from a faucet, the point beyond where the droplet falls from the faucet is the point where the surface tension can no longer sustain the downward pull of the droplet growing in size. Robust methods have been developed [52] to determine the interfacial surface tension between fluid interfaces which rely on

numerically solving variations of the Young-Laplace equation describing pressure jump across a fluid interface, Equation 2.2. These solutions are then compared to an experimental image where adjusting parameters in the numerical scheme will change the profile of the theoretical droplet and converges when the the distance between experimental and numerical curves are minimized. The manipulated parameter, which is the bond number β, is then utilized to determine the interfacial surface tension, Equation 2.10.

$$\Delta P = \gamma(\frac{1}{R_1} + \frac{1}{R_2}) \tag{2.2}$$

where γ is the interfacial surface tension and R_1 and R_2 are the principle radii of curvature at a point on the droplet interface.

The explicit application of this equation and its various forms will be utilized to determine the interfacial tension of a pendant droplet and the fluid in which it is suspended. Figure 2.4 portrays a pendant drop in static equilibrium with its surroundings.

The previous form of the Laplace-Young equation does not take into account the added hydrostatic pressure incurred by the presence of gravity and inherent differences in density when a pendant droplet is suspended within another fluid. The Laplace-Young equation suited for this problem becomes:

$$\Delta P = \Delta P_o - \Delta \rho g z \tag{2.3}$$

where ΔP_o is the pressure at some reference plane on the surface of a droplet in static equilibrium, z is the distance measured upward from this reference plane, $\Delta \rho$ is the difference in fluid densities and g is simply the downward acceleration of gravity, agreeing with the sign convention.

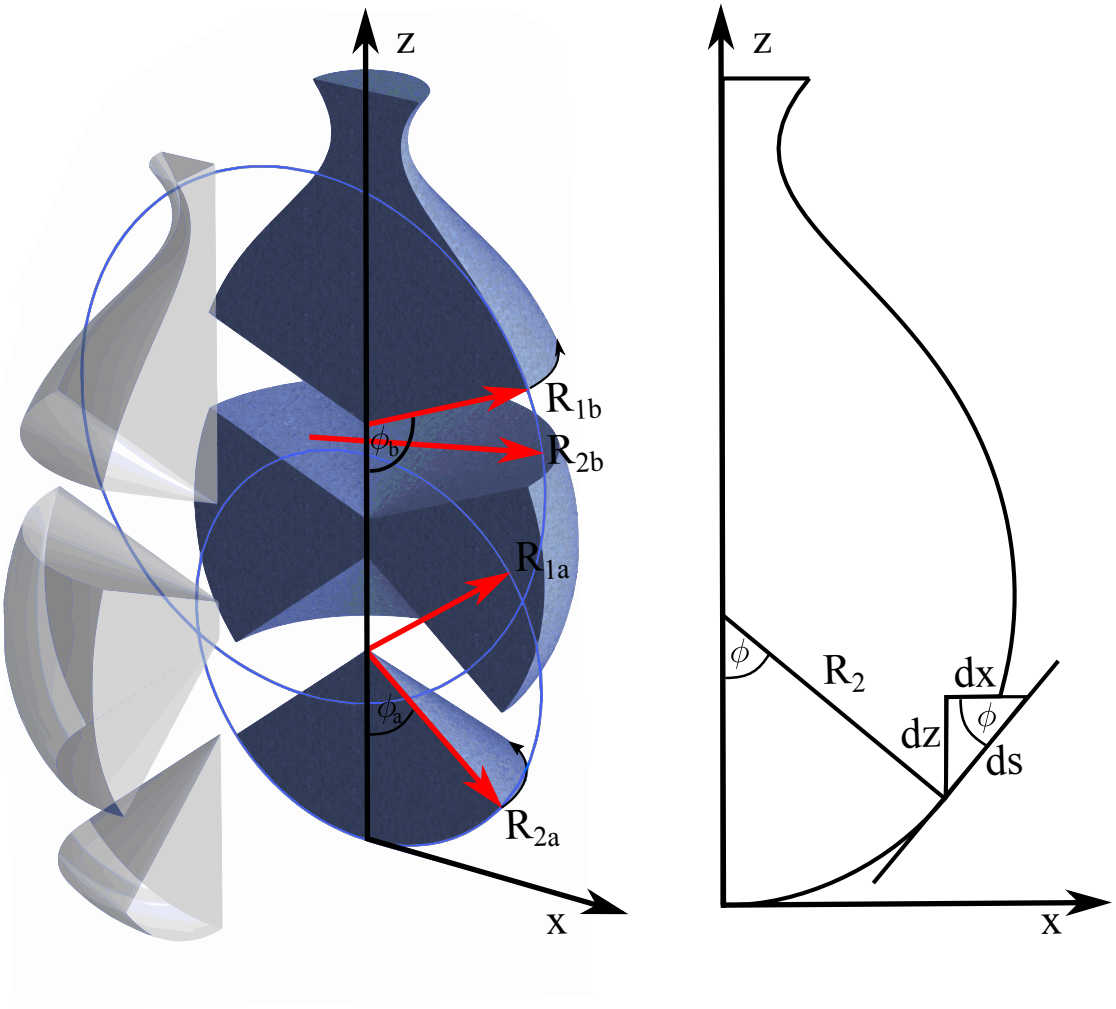

Figure 2.4: Water pendant droplet suspended in air in static equilibrium

ΔP_o can be determined by strategically selecting the reference plane. The reference plane is selected to be the droplet apex. By comparing Equations 2.2 and 2.3 and understanding that at the reference plane, i.e. the apex, the radial curvatures are identical and the z coordinate is zero, ΔP_o becomes:

$$\Delta P_o = \gamma(\frac{1}{R_1 apex} + \frac{1}{R_2 apex}) = \frac{2\gamma}{b} \tag{2.4}$$

where b is the radius of curvature at the apex of the droplet.

Coupling equations 2.2 and 2.3 with the addition of ΔP_o, the resulting form of the Laplace-Young equation is now expressed in terms of the principle radii of the droplet, surface tension, difference in density and some distance z from the origin, Equation 2.5.

$$\gamma(\frac{1}{R_1} + \frac{1}{R_2}) = \frac{2\gamma}{b} - \Delta\rho g z \tag{2.5}$$

This equation is difficult to solve via graphical-numerical methods due to the imaging required to capture the relevant curvatures and the inherent imprecision associated with multiple images and resolving curvatures with pixels. It is therefore necessary to recast this equation into a form fit for coupling and solving numerically. Through some intuitive substitutions, a more useful for can be developed.

R_1 acts about the axis of symmetry and normal to the surface of the droplet and can be rearranged in terms of its projection onto the x axis and the tangential angle, ϕ, formed with the x axis, Equation 2.6. R_2 can be expressed in terms of the rate of change of the tangential angle ϕ with respect to the arc length s, referred to as the local curvature k, Equation 2.7.

$$\frac{1}{R_1} = \frac{\partial\phi}{\partial s} \tag{2.6}$$

$$\frac{1}{R_2} = \frac{\sin\phi}{x} \tag{2.7}$$

Substitution into Equation 2.5 yields:

$$\frac{\partial \phi}{\partial s} = \frac{2}{b} - \frac{\Delta \rho g z}{\gamma} - \frac{\sin \phi}{x} \tag{2.8}$$

Multiplying 2.8 by b and normalizing the length terms by b

$$\frac{\partial \phi}{\partial s^*} = 2 - \beta z^* - \frac{\sin \phi}{x^*} \tag{2.9}$$

where β is referred to as the Bond number and the asterisk denotes the nondimensional forms of the length parameters, Equation 2.10.

$$\beta = \frac{b^2 \Delta \rho g}{\gamma},\ s^* = \frac{s}{b},\ x^* = \frac{x}{b},\ z^* = \frac{z}{b} \tag{2.10}$$

The Bond Number, β

The bond number is a nondimensional term quantifying the relative effects of gravitational and surface tension forces. One would expect that as gravitational forces dominate, $\beta \sim large$, the droplet would elongate and deform under the pull of gravity due to its greater density and vice versa for surface tension forces when the droplet resists the pull of gravity and remains spherical. For surface tension, with units of $\frac{energy}{area}$, to remain constant for a large droplet, more energy is required to account for its larger area; since all matter seeks its ground state, the lowest energy form for a droplet is spherical, i.e. when the surface area in minimized. For this reason, the shape of a pendant droplet for $\beta \sim small$ is spherical and elongated when $\beta \sim large$ as gravity works against the restoring surface tension forces.

Numerical Solution of Laplace-Young Equation

Referring to Figure 2.4, changes in the x and z directions as well as tangential angle, ϕ, can be related to the change in arc length, s, Equations 2.11.

$$\begin{aligned} \frac{\partial x^*}{\partial s^*} &= \cos\phi \\ \frac{\partial z^*}{\partial s^*} &= \sin\phi \end{aligned} \tag{2.11}$$

Equations 2.9 and 2.11 demonstrate coupling through changes in s^*. By definging some vector y containing the independent variables x^*, z^*, ϕ, the solution to the Laplace-Young equation in cartesian coordinates can be determined through the use of a 4th and 5th order Runge-Kutta routine. Equations 2.12 and 2.13 define the inputs into MATLABs ODE45.

$$y = \begin{bmatrix} x^* \\ z^* \\ \phi \end{bmatrix} \tag{2.12}$$

and from eq. 2.9 and 2.11

$$\frac{\partial y}{\partial s^*} = \begin{bmatrix} \frac{\partial x^*}{\partial s^*} \\ \frac{\partial z^*}{\partial s^*} \\ \frac{\partial \phi}{\partial s^*} \end{bmatrix} = \begin{bmatrix} \cos y_3 \\ \sin y_3 \\ 2 - \beta y_2 - \frac{\sin y_3}{y_1} \end{bmatrix} \tag{2.13}$$

made subject to the boundary conditions at the droplet apex:

$$x^* = z^* = \phi = 0 \tag{2.14}$$

Figure 2.5 illustrates the intermediate steps in the solution procedure.

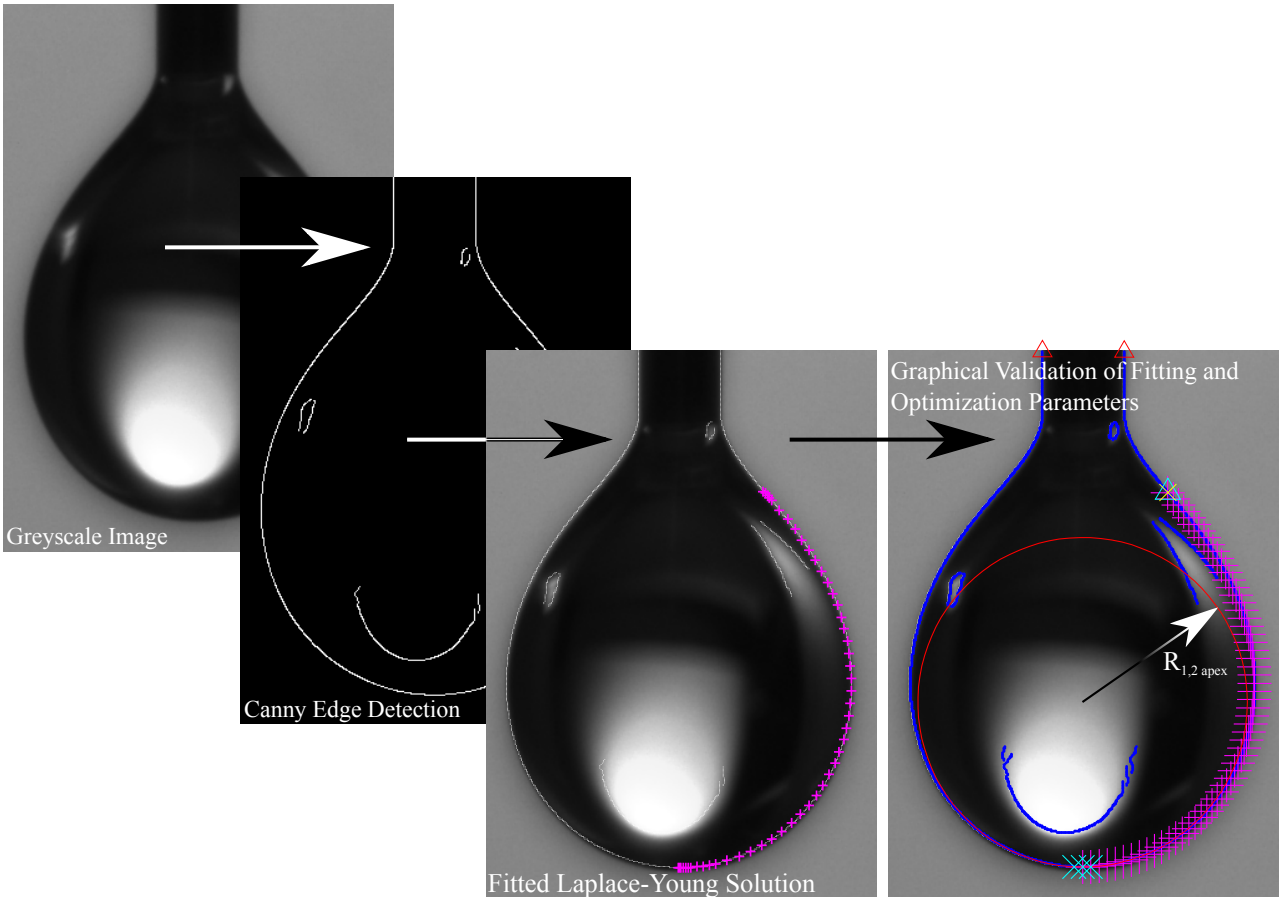

Figure 2.5: Work flow for the processing of an experimental image of a pendant drop.

The experimental image is converted to binary through the Canny edge detection method. Critical locations such as the points of the needle from which the droplet is suspended are utilized to provide dimensionality. The numerical solution is then compared to the edge in the image where

the Bond number is adjusted iteratively until a least squares algorithm returns a minima where the Bond number is then rearranged to determine the interfacial tension, γ.

Microchannel Design

Poly(dimethylsiloxane), also known as PDMS, was chosen as the microchannel material. This material is a type of two-part polymer that is mixed and cured to produce a trans- parent elastomer. PDMS offers many advantages as a microfluidic device due to its inert physical properties. The bulk material is also naturally hydrophilic to aqueous solvents. Since the plasma treatment process used to bond solid PDMS to PDMS causes the microchannel surfaces to become hydrophilic to aqueous liquids, the chips are heat treated to make them hydrophobic. Typical heat treatment is for 2-4hrs at 180^oC.

This section contains the details of the specific microchannel geometry molded into the microfluidic chip. The geometry required for this study is a T-junction, as shown in Figure 1.1. Specific dimensions were chosen to keep the flow laminar to achieve fully developed flow. The Reynolds number range based on the channel dimensions, fluids properties, and flow rates chosen for this study was from 0.01 to $\sim$ 25, well within the laminar flow regime. The laminar entry length required to achieve fully developed flow for these same parameters is $0.1\mu m$-$190\mu m$. The fluids considered for this preliminary analysis are silicone oil (PMX-200, Dow Corning) and nanosuspensions of alumina. The entry length requirement to reach a fully developed laminar flow is satisfied by allowing $5mm$ of channel length after the inlet ports and before the T-junction. In addition, providing $10mm$ of channel length after the T-junction allows for adequate imaging. Figure 2.6 shows the dimensions of an individual microchannel and Figure 2.7 shows the full chip with all five microchannels. Table 2.1 lists the relevant material properties and flow conditions for the fluid pairs utilized for the current study defined in Figure 1.1.

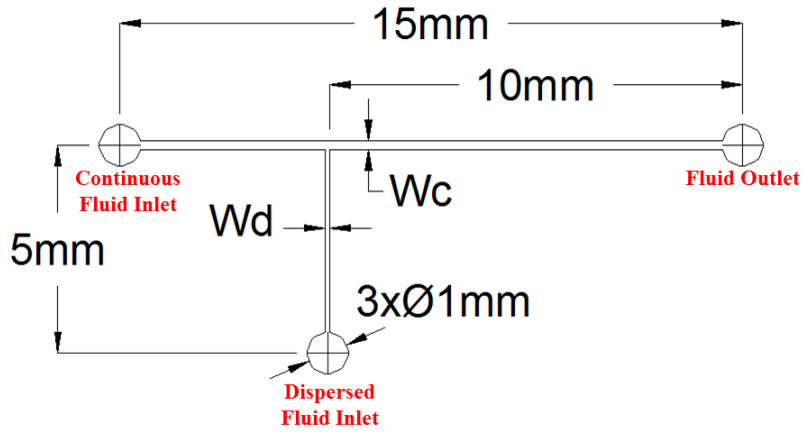

Figure 2.6: T-junction microchannel geometry.

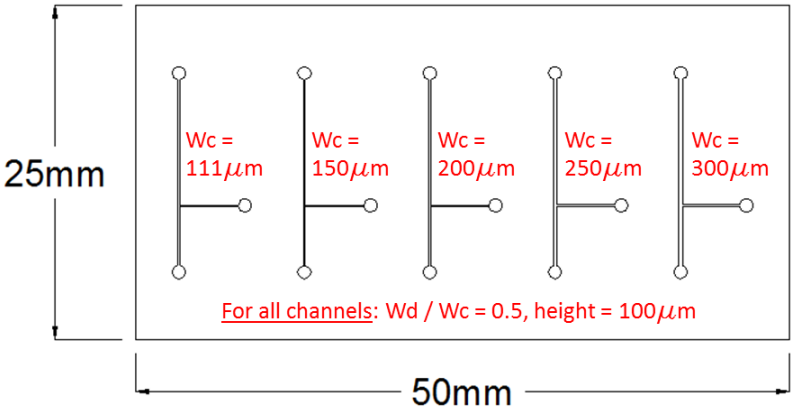

Figure 2.7: Full chip design with five T-junction microchannels of varying widths.

Table 2.1: Properties of fluid pairings.

Dispersed Phase	Continuous Phase	γ (mN/m)	λ	Γ
10% $20nm$ Al_2O_3	$20cSt$ Silicone Oil	9.6	1.0	0.5
6.4% $30nm$ CuO	$20cSt$ Silicone Oil	26.2	0.37	0.5

Experimental Procedure

This section outlines the testing procedures and standards required to produce accurate and repeatable data. Material contamination risk and material handling procedures are also presented in order to prevent inconsistencies in data.

Fluid Delivery to MFD and Handling Practices

Delivering fluid to the MFD requires equipment with the precision and resolution necessary to be able to produce a variety of flow structures with the ability to maintain steady state conditions. The tool most commonly used for such applications is the stepper motor or syringe pump. Often times these devices come pre-programmed with information regarding commercially available syringes, e.g. Terumo brand 5, 6 and $10cc$ syringes. The syringes are filled by the user with the desired fluid and then loaded into the pump. The pump is then operated manually by the user or reads a script containing ASCII commands generated by the user to perform a set of operations at specified intervals and flow rates. The syringes are mounted to the syringe pump and connected to the MFD via Tygon brand tubing. The tubing is transparent and quite flexible which is conducive to troubleshooting blockages and visualizing the fluid flowing within. Stainless steel Luer lock needle attachments were re-purposed by removing the stainless steel tips which fit inside the Tygon tubing. The needles are then attached to the MFD where the fluid is channeled at the prescribed flow rate to the T-junction. This setup can be seen in Figure 2.8.

Time Dependence of Stable Droplet Production

Most engineering systems utilizing fluid flow or heat transfer often times are faced with transients or variations in response as a system reaches equilibrium due to an imbalance of energy supplied

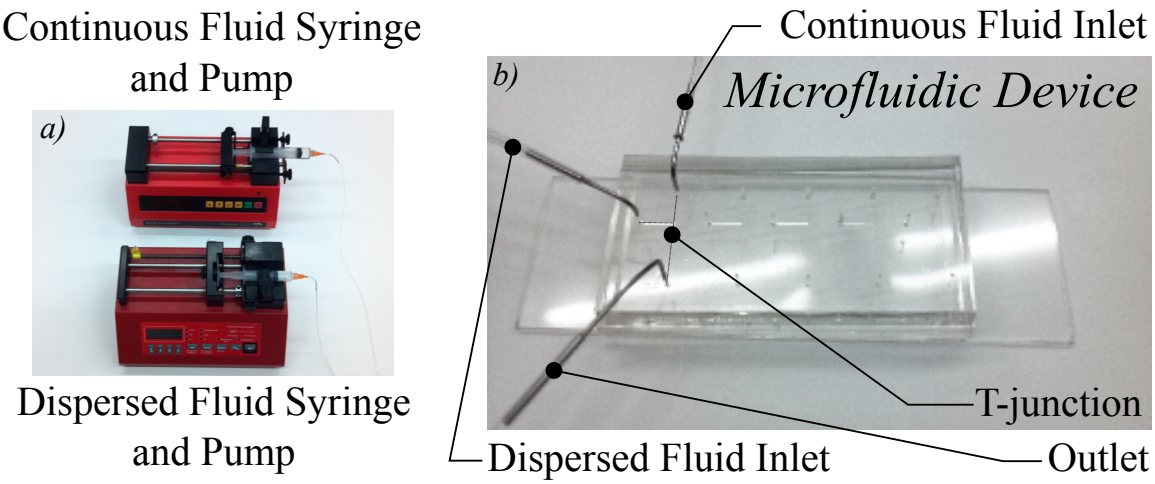

Figure 2.8: a) Syringe pumps with continuous and disperse fluids loaded. b) Microfluidic device containing T-junction utilized in experiment showing the manner in which the tubing is connected.

to and taken from the system. In the case of MFD's, transients on the order of $30min$ are not uncommon especially for low flow rates [2]. Garstecki *et al.* [2] reported equilibrium times occurring on the order of seconds for high flow rates ($\sim$ 1-10$\mu L/s$) and up to 1-30min for low flow rates ($\sim$ 10^{-4}-$10^{-2}\mu L/s$). In the case of this study, low flow rates on the order of $\sim$ 10^{-3}-$10^{-1}\mu L/s$ were utilized and required upwards of $20min$ to stabilize each time the flow rate was adjusted. Other factors add to this time dependent problem such as the length of tubing utilized. Longer lengths of tubing generate greater pressure head. This pressure works on the flexible rubber tubing, causing it to expand. Expansions such as these prevent the prescribed volumetric flow rate from reaching the T-junction as soon as the flow rate increases. Once the MFD and tubing cease to deform and pressures within the system stabilize, accurate measurements are then possible.

Fluid Handling Practices

Producing monodisperse droplets in a MFD with predictability requires extensive precautionary measures resulting from the sensitivity of interfacial tension to contamination. In the case of large

scale applications, i.e $Re >> 1$, fluid contamination becomes less of a concern as small amounts of particles or contaminants typically have little effect on properties such as viscosity or density. For the case of this study, $Re << 1$, indicating a dependence on interfacial tension for a two phase system, a material property that is heavily dependent upon surface chemistry.

In an experiment designed to validate the presence of contaminants, a Terumo syringe was used direclty out of the sterile packaging to suspend a droplet of water in air. The pendant drop method was utilized to determine the interfacial tension to be $68.9mN/m$. The same experiment was repeated for a syring cleaned with soap and sonicated in DI water multiple times. The results of this experiment returned an interfacial tension of $71.9mN/m$ which is within 1% of the accepted value at room temperature. These discrepancies in the accepted values and experimentally determined values can lead to variations in the capillary number and as a result, a bias in the data collected for that pair of fluids. Therefore, interfacial tension for each fluid pair was determined via the pendant drop method where the droplet was produced using the same equipment used in the experiment to produce droplets. For the sake of producing data consistent with the literature, clean handling and equipment cleanliness practices have been observed. Gloves and thoroughly washed beakers were utilized to transport fluids. Fluid contact surfaces such as the inner barrel of the fluid syringe were washed and dried before carrying fluids. With these precautions and adequate material characterization procedures, the production of accurate and repeatable rate was readily achievable.

Visualization and Data Acquisition

Droplet production rates in a MFD typically occur faster than our ability to interpret and resolve shape or even structure of the flow for high capillary numbers. Imaging devices are capable of recording video at frame rates high enough to resolve the process of break up and the trajectory of the droplet downstream. Visualization equipment utilized for this study consist of a microscope, a

focusing lens and camera capable of streaming data to a PC equipped with software designed for video streaming. The experimental setup is shown below in Figure 2.9.

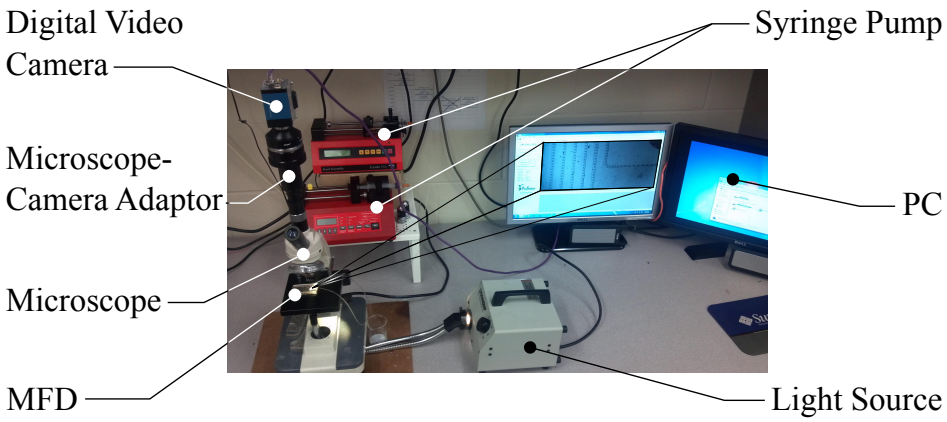

Figure 2.9: Microscope, Light source, camera and PC utilized for experimentation.

This configuration allows for the live streaming of the T-junction on the PC for data acquisition giving the user greater control over more variables where peering through the eyepiece of the microscope to evaluate the flow structure is no longer necessary.

Targeting Specific Flow Structures and Regimes

Without first characterizing the flow regimes for a specific geometric configuration and set of fluids, predicting droplet production characteristics becomes guesswork. It is necessary to understand transitional regimes in order to predictably produce monodisperse droplets of desired size.

Correlations and Transitional Values

Gupta *et al.* [16] presented a comprehensive study identifying the transitions between flow regimes in a T-junction. The work outlined for a range of Capillary numbers, flow rate ratios corresponding

to production regime transitions. Droplet at T-junction (DTJ), Droplet in channel (DC) and Parallel flow (PF) were the main regimes of droplet production considered. DTJ is the formation of a droplet at the T-junction where DC is characterized by the formation of a thread that extends downstream until instabilities cause the thread to form droplets. In the case of the study, DTJ transitions to DC and DC to PF where PF is characterized by the thread forming in DC extends beyond the domain of consideration.

Confined vs. Un-confined

Droplet confinement occurs when a droplet makes contact with MFD channel walls. This type of droplet formation is characteristic in low Capillary number flows where pressure drives droplet breakup at the T-junction and for some cases of high disperse phase flow rates. A droplet not experiencing geometric confinement is subject to deformation due to shear flow where elongation can occur for large droplets relative to the characteristic dimensions of the MFD.

CHAPTER 3: Results and Discussion

Solids Structures from Colloidal Suspensions and Heat Transfer

Through the use of aqueous suspensions of alumina dispersed in oil, the production of spherical solids is possible with some reduction in size due to Precipitation Induced Diametral Regression. These solid particles diminish in size over time with increasing particle concentration relative to the dispersing medium when heated near the saturation temperature of the dispersing medium.

Preliminary tests were conducted to demonstrate the effect of particle concentration on the magnitude of diameter regression. The test consisted of suspending a pendant droplet at various concentrations of alumina in a heated oil bath at 95^oC. The static droplet was heated and video acquisition proceeded until droplet size ceased to change. Figure 3.2 illustrates the transition of the droplet profile over time for $\sim 10\%$ alumina in water.

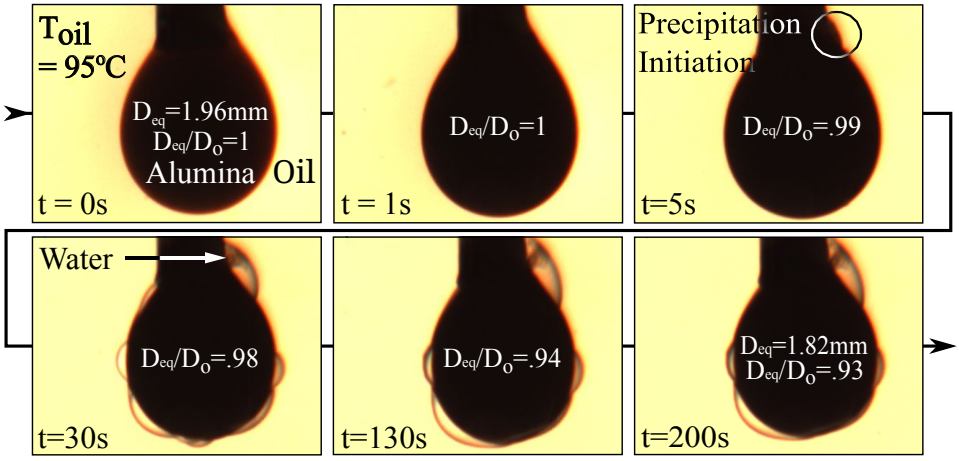

Figure 3.1: Regression of droplet diameter over time. Alumina initially at $\sim 10\%$ volume concentration and 25^oC dispersed in $20cSt$ PDMS Oil heated between 90-100^oC.

The equivalent diameter of the droplet decreases over time as the droplet continues to heat. The

equivalent diameter is determined by calculating the volume of the droplet image numerically and comparing that value to the volume of a sphere of *equivalent diameter*. The test was conducted for $\sim 10\%$, 7%, 5% 3% and 1%. The normalized equivalent diameters (equivalent diameter, D_{eq} normalized by initial equivalent diameter D_o) are plotted against time for various concentrations, Figure 3.2.

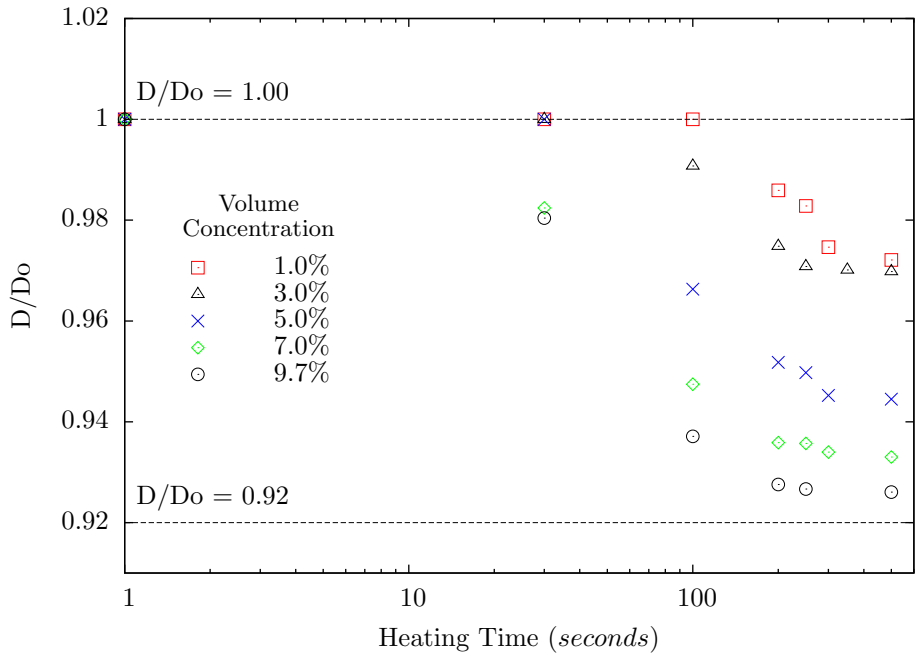

Figure 3.2: Regression envelope formed as the droplets similar to those in Figure 3.1 contracts from the initial equivalent diameter, D_o, to the final equivalent diameter, D_f.

Mechanisms of Solidification

Considering the EISA mechanisms utilized to produce solids noted in the introduction [47], the current study considers thermal diffusion into the liquid droplet, the diffusion of nanoparticles within the droplet and the formation of agglomerates beginning at the liquid/liquid interface progressing inward to form the resulting solid particle. The mechanisms governing the solidification

process are considerably different given that the dispersing medium for the nanoparticles in this study is not miscible with the continuous carrier fluid. In [47], agglomeration was the result of dominating time scales. The study identified time scales associated with both particle diffusion and also the dispersing fluid *evaporating* into the continuous carrier fluid. For cases where rates of particle diffusion were dominated by suspending fluid evaporation, the particles had an insufficient amount of time to redistribute in the droplet and as a result agglomerated at the shrinking liquid/liquid interface forming a shell structure.

The current study proposes a mechanism for solidification governed by colloidal chemistry called Temperature Induced Forming. The physics of the problem are described by transient heat conduction and particle diffusion. The particle/particle interactions, shown in Figure3.3 occur as a result of increasing temperature. Additional phenomenon such as precipitation of the dispersing fluid to the liquid/liquid interface as shown in Figure 3.1 occurs similar to the study conducted by Fang *et al.* [43]; however, the dispersing fluid and continuous carrier fluid in this study are immiscible. There appears to be a competition between Heat Induced Precipitation of the dispersing medium and the agglomeration of alumina particles resulting from TIF.

Temperature Induced Forming

TIF relies on a sterically and electrostatically stabilized suspensions of nanoparticles ability to dissociate and form ions at elevated temperatures. In the case of TIF, alumina particles are suspended with negatively charged dispersing agent that adheres to the surface of the particle along with negatively charged polymeric dispersant. The alumina sheds positive Al ions while in aqueous suspension as temperature increases, taking with it the negatively charged dispersing agent, leaving behind a positive surface site on the alumina particle. This shedding of ions reduces the magnitude of the EDL repulsive forces and aids in the initiation of flocculation similar to the

mechanism contributing to DCC. This method, however, differs from other methods in that the polymeric stabilizer in suspension with negatively charged sites adheres to the newly developed positively charged surface site on the alumina particle due to the dissociation of the Al ion. This progresses throughout the solution until and beyond the point when flocculation ensues. The result is a solid green body in an irreversible flocculated state [45]. Figure 3.3 (Adapted from [45]) outlines the TIF process described above.

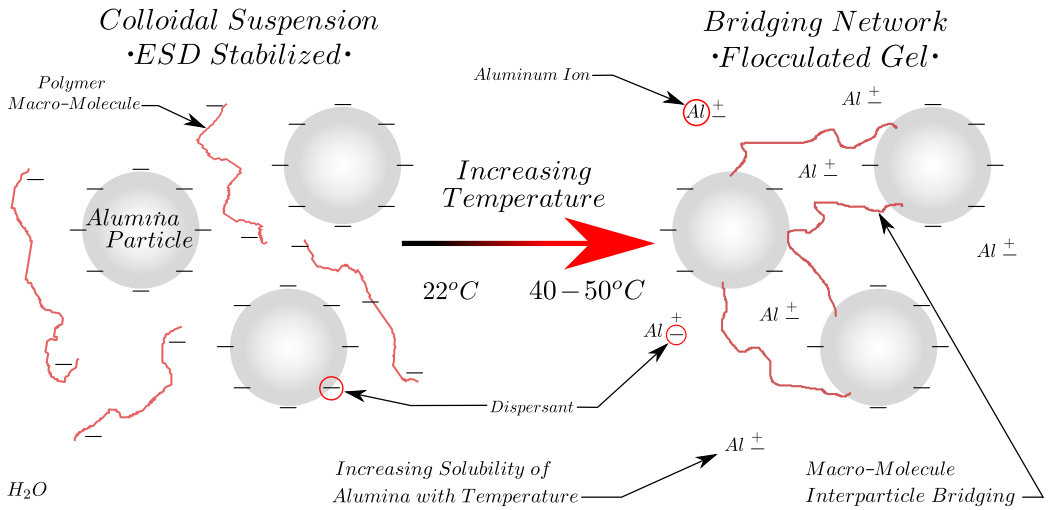

Figure 3.3: Formation of polymeric bridging network in aqueous alumina suspension

This process indicates a transition from a stable nanoparticle suspension resulting from steric and ESD forces to an unstable suspension consisting of linked particle-particle networks. In this unstable flocculated state, the ESD forces have been nullified by the ionizing of the alumina and the formation of inter particle bridges which bring the particles closer together. The proximity of the particles tends toward increases in the van der Walls attractive forces as suggested by the DLVO theory and finally, the steric repulsive forces contributed by the surfactant transition to flocculation through its role as the inter-particle bridging mechanism at the elevated temperatures.

It is proposed that both Heat Induced Precipitation and TIF will result in a solid structure of alumina

particles since this evaporation has previously been shown to produce solids [53]. The addition of precipitation in the solidification process acts to decrease the equivalent diameter of the droplets shown in Figure 3.1 since precipitation is a precursor the diametral regression. The experiment was repeated to obtain additional support for this arguement. However, the heating temperature of 60^oC is enough to induce solidification due to TIF but low enough such that precipitation never occurs for the time scales considered in the previous experiment. This experiment also demonstrated that the TIF process alone may not be sufficient to cause a change in droplet size. These artifacts support an argument for solidification resulting from TIF and Precipitation Induced Diametral Regression.

This study seeks the production of monodisperse microspheres consisting of gelled alumina particles referred to as solids. It is for this reason that temperatures utilized to produce solids are high enough to produce solid structures but below the saturation temperature of the dispersing fluid.

Material Characterization of Aqueous Suspensions

Aqueous suspensions of $20nm$ alumina with dispersant and $30nm$ copper oxide aqueous suspension with dispersant were acquired from nanophase Technologies Corporation.

For use within the MFD, material characterization practices were executed as discussed in previous sections in order to map and predict droplet formation characteristics.

Typically, aqueous suspensions containing only alumina, i.e. in the absence of surfactant, and also for low volume concentrations ($\sim< 40\%$) have been shown [51] to demonstrate viscosity variation inversely with temperature, attributed primarily to the aqueous dispersing medium. In this case, viscosity decreases and levels off asymptotically beyond high temperatures without any sudden transition in viscosity corresponding to a specific temperature range. Experiments with alumina and CuO suspensions have demonstrated typical temperature dependent properties, e.g. viscosity,

for a range of temperatures up to about 40^oC, beyond which, viscosity increases exponentially. The temperature dependent viscosity curves for the aforementioned suspensions demonstrate a local minimum in the range of 40^oC-50^oC. These points will be referred to as the points of solidification and are 45^oC and 49^oC for alumina and CuO respectively, Figure 3.4.

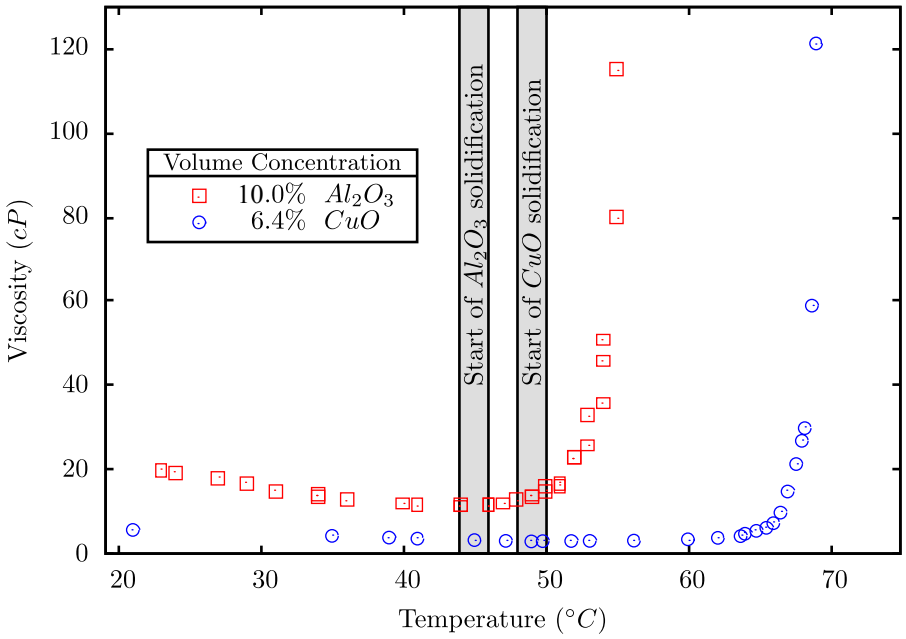

Figure 3.4: Viscosity vs. temperature of $\sim 10\%$ volume concentration alumina and 6.4% volume concentration copper oxide at a shear rate of $20s^{-1}$

Understanding and developing the techniques implemented to cause this increase in viscosity has given rise to significant increase in efforts in the field of colloidal sciences. Studies conducted by Yang *et al.* [51] were focused on TIF and the determination of the gelation threshold for aqueous suspensions of alumina with polyacrylic acid (PAA) as dispersant which led ultimately to solidification. Further studies [54] show a similar trend by the addition of PAA, tri-ammonium citrate and magnesium citrate powders. Thorough material characterization in this study also resulted in determining the bounds of volume concentrations for the alumina suspension for a fixed viscometer shear rate of $20s^{-1}$. Figure 3.5 below illustrates the temperature dependence of viscosity for var-

ious volume concentrations of alumina. It is evident that for some volume concentration between 1% and 6%, a gelation threshold exists below which, solidification will not develop.

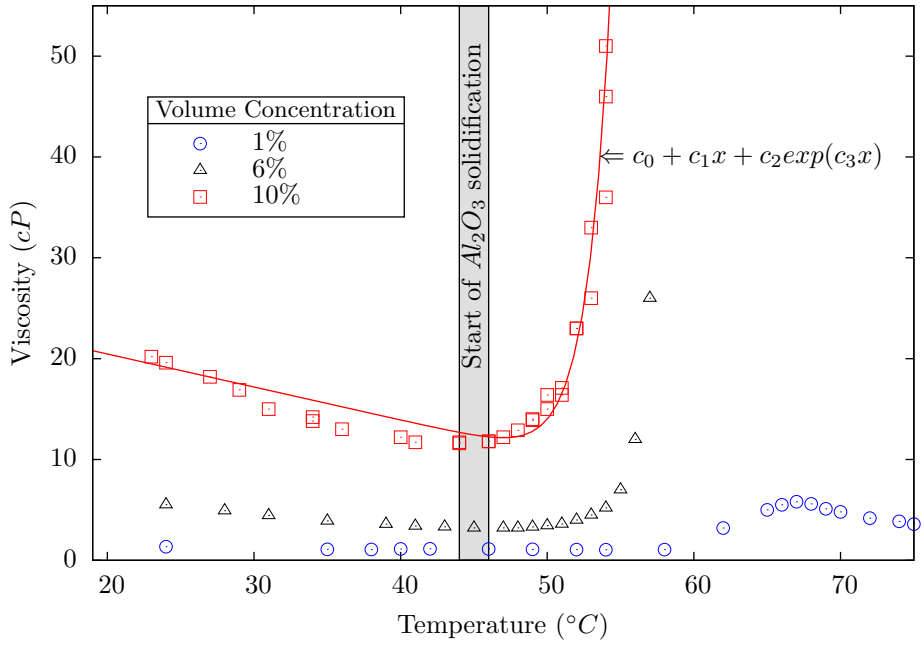

Figure 3.5: Viscosity variation with temperature for various concentrations of alumina at a shear rate of $20s^{-1}$

As mentioned above, a gellation threshold exists where for the 1% volume concentration bridging flocculation initiated as there exists a slight upswing in viscosity around 60^oC; however, the bridges formed are too few to retard the shearing of the viscometer to register as a further increase in viscosity. The particle-particle networks formed in this case break into smaller flocs and precipitate from suspension as was observed by semi-solid chunks at the bottom of the measurement device. This evidence suggests a high probability that the surfactant used in the manufacture of the alumina and CuO suspensions for this study are polymeric in nature and fits within the group of surfactants capable of TIF.

With an understanding of TIF and the suspensions characterized above, this study seeks to utilize these fluids in a MFD to produce solid particles via TIF.

Experimental Specifications

The MFD utilized, Figure 1.1b, to produce solid particles was a T-junction of characteristic dimensions, Figure 1.1, $w_d = 75\mu m$, $w_c = 150\mu m$, $h = 100\mu m$ (channel depth throughout device represented as the depth into the page), $Q_c = 1000\mu L/hr$ and $Q_d \sim 100\mu L/hr$. The dispersed phase corresponding to the subscript d was the $\sim 10\%$ alumina suspension described above and the continuous phase, c, was $20cSt$ PDMS Oil manufactured by Sigma-Aldrich. This fluid pair exhibit similar viscosities $\sim 20cP$ and an interfacial tension measured in house via ASDSA (pendant drop method) written in MATLAB of $9.6mN/m \pm 1mN/m$.

The fluids were pumped at the desired flow rate by two syringe pumps running simultaneously (World Precision Industries, Sarasota, FL Model: AL-1000HP and Kent Scientific, Torrington, Ct Model: Genie Plus) equipped with $5cm^3$ and $10cm^3$ Terumo syringes for dispersed and continuous fluids respectively.

The PDMS T-junction utilized in this study was manufactured by the Stanford Microfluidics Foundry through a process referred to as soft lithography. This process has been presented in great detail elsewhere [55].

A spot heater was used to heat the microchannel and the droplets generated within. A copper stud was heated at its base and made contact with the modified solid PDMS Micro-channel at the other end. The heat conducted through the solid PDMS to the microchannel then transferred convectively from the PDMS oil into the droplets resulting in solidification. Excess Material was trimmed from the solid PDMS to reduce the distance between the copper stud and the microchannel, exaggerated in Figure 3.6a. The two phase suspension of the PDMS Oil and alumina microspheres were collected at the end of the copper stud in a petri-dish that facilitated observation under a microscope, as shown in Figure 3.6a and 3.6b. The resulting solids were imaged and sized

as shown in Figure 3.6c.

Results: Experimental Solidification in situ

Utilizing a flow rate ratio $\frac{Q_d}{Q_c} = 0.1$ with a continuous flow rate of $1000\mu L/hr$ and the above noted experimental setup, alumina particles ranging in size from $10\mu m$-$40\mu m$ were produced with an average size of $30\mu m$ and were collected from the copper structure, Figure 3.6a and 3.6b. Initially, both the dispersed and continuous fluids at the T-junction were at room temperature. Downstream, in the heat affected region approximately $7mm$ from the junction, the droplet was heated until it reached an approximate outlet temperature of 60^oC-80^oC, beyond the solidification temperature for the alumina nanosuspension. The following section discusses the basis upon which approximate temperatures are determined.

Simulation Results: Temperature Distribution in the Microchannel

Numerical simulations of the single phase oil flow were conducted in COMSOL to determine the temperature profile in the microchannel for the conditions used in the experiment. For these simulations, the dispersed phase (alumina droplets) was not included. COMSOL is a finite element simulation package in which the microchannel geometry, flow physics, meshing, and post processing can be executed. For this study, a steady state laminar single phase flow simulation coupled with heat transfer in both the solid wall and liquid was implemented to produce temperature along the centerline of the channel. The temperature dependence of the $20cSt$ PDMS Oil viscosity was measured in house through the processes outlined in preceding sections and the data were curve-fitted using MATLAB. The resulting fit was utilized in the COMSOL solution parameter environment as the fluid viscosity. Manufacturer specified density at various temperatures and a linear curve fit was generated in the same manner and passed to COMSOL for simulation. The resulting kinematic

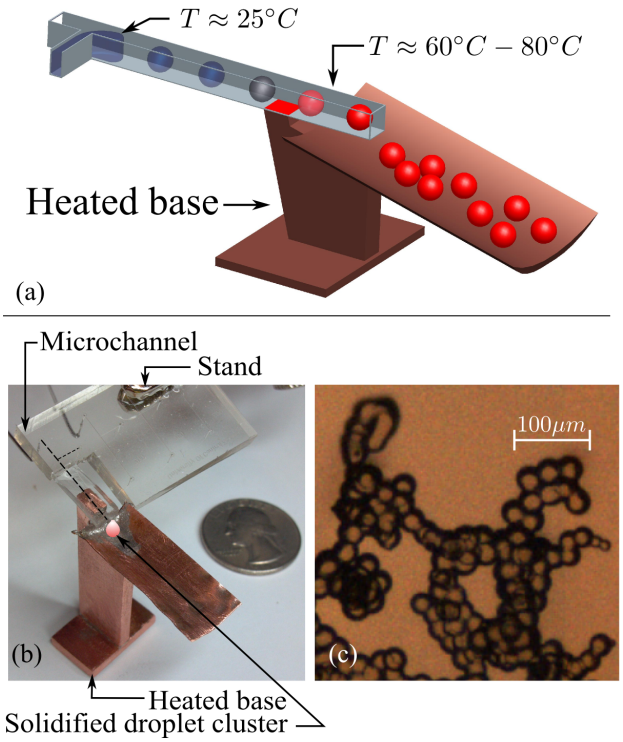

Figure 3.6: a) Conceptual representation of the manufacturing configuration, b) experimental setup with illustration of pendant drop formation containing microspheres, c) microscope image of solid alumina particles.

viscosity in the simulation as a function of temperature along the centerline of the micro-channel was validated by comparison to hand calculations and was found to be within $\sim 1\%$. The simulation results represent a steady state solution of $20cSt$ PDMS Oil flowing through a heated channel of identical dimensions and heater temperature. This numerical procedure provides a temperature distribution of the centerline of the microchannel. With this numerical temperature distribution, the viscosity of an alumina droplet can be predicted and consequently, solidification can be predicted through the simulation. Figure 3.7 presents the results of the simulation in a cross sectional temperature plot of the microchannel. Temperature along the centerline is plotted, each temperature value is also passed to the curve fit generated from the alumina viscosity vs temperature data shown in Figure 3.5 for $\sim 10\%$ volume concentration. The 2D plot is aligned with the fringe plot above and illustrates the evolution of temperature along the centerline due to the addition of heat from

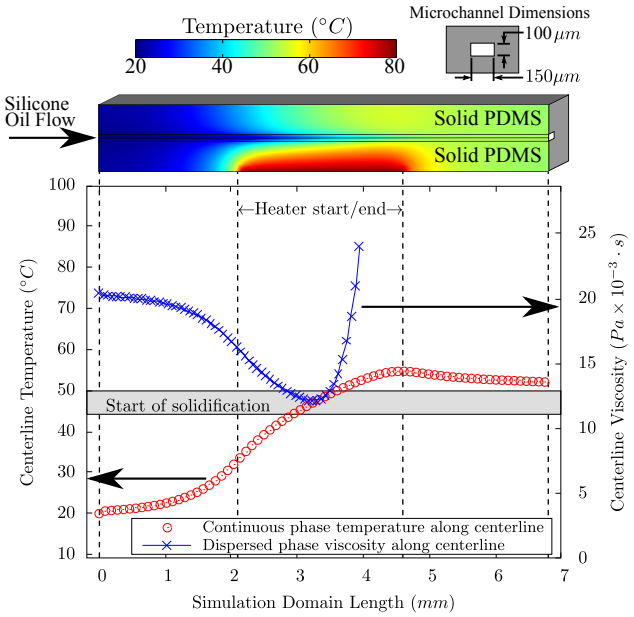

Figure 3.7: COMSOL simulation of heated portion of the micro-channel. Centerline temperature is plotted as a function of centerline displacement. Alumina suspension viscosity is plotted as a function of centerline temperature. The fringe plot of the temperature distribution of the simulated domain is shown at top along with temperature color bar.

the copper stud. This information allows the consideration of a scenario where a droplet containing temperature sensitive suspensions of alumina is passed through the heated domain. Utilizing the temperature profile generated by the simulation, it can be seen that as this theoretical droplet approaches the heated section, it begins to rise in temperature as a result of conduction upstream through the solid PDMS which heats the silicon oil. Once the droplet enters the heated section, temperatures are estimated to approach the solidification temperature for the alumina suspension of 45^oC. By the time the droplet passes the heated section of the channel, it encounters temperatures greater than the solidification temperature, and hence, reaches a fully gelled solid state. As mentioned above, the measure of viscosity change of the alumina suspension can represented by utilizing the curve fit developed from experimental data and is the blue curve plotted along the centerline. The grey bar is offered as an indicator of solidification as the temperature reaches the

solidification temperature value at $\sim 3mm$ along the centerline displacement; it is shown that viscosity will increase as a result of this critical temperature and consequently, displacement along the centerline.

CHAPTER 4: CONCLUSION

This thesis reports the first study of its kind in generating droplets in a T-junction using two immiscible fluids, and solidifying them into microstructures through a process called Temperature Induced Forming (TIF). A microfluidic T-junction ($w_d = 75\mu m$, $w_c = 150\mu m$ and $h = 100\mu m$) was used to produce nanoalumina droplets. Formation of such a droplet occurs as a result of a balance of distorting viscous shear and pressure forces imposed on the dispersed fluid (nanoalumina) by the continuous fluid (silicon oil) and restoring interfacial tension forces. The viscosity of nanoalumina at different concentrations was measured across a range of temperatures beyond the inception of the solidification temperature. To measure the interfacial tension between nanoalumina fluid and silicone oil, a graphical method was utilized. Using the Young-Laplace equation and the image of a nanoalumina pendant droplet in silicone oil, interfacial tension was measured by solving the Young-Laplace equation numerically and fitting it to the experimental image. This was done by iteratively changing the Bond number and solving for interfacial tension. Nanoparticle suspensions of alumina in water dispersed with polymeric macromolecule exhibit unique viscosity characteristics at the gelation temperature. Viscosity is shown to increase with temperature beyond the gelation temperature of 40^oC-50^oC until the point of solidification (TIF). Preliminary low solid concentration experiments (1%-10% volume concentration of alumina in H_2O) have indicated solidification and a regression in droplet diameter when heated near the saturation temperature of the water used to disperse the particles. The microstructures formed in the microfluidic device by this solidification process are uniform and are estimated to be $30\mu m$ in size.

APPENDIX A: LIST OF REFERENCES

[1] T. Thorsen, R.W. Roberts, F.H. Arnold, and S.R. Quake. Dynamic pattern formation in a vesicle-generating microfluidic device. *Physical review letters*, 86(18):4163–4166, 2001.

[2] Piotr Garstecki, Michael J Fuerstman, Howard A Stone, and George M Whitesides. Formation of droplets and bubbles in a microfluidic t-junction-scaling and mechanisms of break-up. *Lab on a Chip*, 6(3):437–446, 2006.

[3] GF Christopher and SL Anna. Microfluidic methods for generating continuous droplet streams. *Journal of Physics D: Applied Physics*, 40(19):R319, 2007.

[4] G.F. Christopher, N.N. Noharuddin, J.A. Taylor, and S.L. Anna. Experimental observations of the squeezing-to-dripping transition in t-shaped microfluidic junctions. *Physical Review E*, 78(3):036317, 2008.

[5] JH Xu, SW Li, J. Tan, and GS Luo. Correlations of droplet formation in t-junction microfluidic devices: from squeezing to dripping. *Microfluidics and nanofluidics*, 5(6):711–717, 2008.

[6] T. Fu, Y. Ma, D. Funfschilling, C. Zhu, and H.Z. Li. Squeezing-to-dripping transition for bubble formation in a microfluidic t-junction. *Chemical Engineering Science*, 65(12):3739–3748, 2010.

[7] D.M. Fries and P. Rudolf von Rohr. Impact of inlet design on mass transfer in gas–liquid rectangular microchannels. *Microfluidics and nanofluidics*, 6(1):27–35, 2009.

[8] S. Van der Graaf, T. Nisisako, C. Schroen, RGM Van Der Sman, and RM Boom. Lattice boltzmann simulations of droplet formation in a t-shaped microchannel. *Langmuir*, 22(9):4144–4152, 2006.

[9] K. Wang, YC Lu, JH Xu, and GS Luo. Determination of dynamic interfacial tension and its effect on droplet formation in the t-shaped microdispersion process. *Langmuir*, 25(4):2153–2158, 2009.

[10] Y. Zhang and L. Wang. Experimental investigation of bubble formation in a microfluidic t-shaped junction. *Nanoscale and Microscale Thermophysical Engineering*, 13(4):228–242, 2009.

[11] L. Dai, W. Cai, and F. Xin. Numerical study on bubble formation of a gas-liquid flow in a t-junction microchannel. *Chemical engineering & technology*, 32(12):1984–1991, 2009.

[12] M De Menech, P Garstecki, F Jousse, and HA Stone. Transition from squeezing to dripping in a microfluidic t-shaped junction. *Journal of Fluid Mechanics*, 595(1):141–161, 2008.

[13] C. Paquet, Z.J. Jakubek, and B. Simard. Superparamagnetic microspheres with controlled macroporosity generated in microfluidic devices. *ACS Applied Materials & Interfaces*, 2012.

[14] S. Xu, Z. Nie, M. Seo, P. Lewis, E. Kumacheva, H.A. Stone, P. Garstecki, D.B. Weibel, I. Gitlin, and G.M. Whitesides. Generation of monodisperse particles by using microfluidics: control over size, shape, and composition. *Angewandte Chemie*, 117(5):734–738, 2004.

[15] Amit Gupta, SM Murshed, and Ranganathan Kumar. Droplet formation and stability of flows in a microfluidic t-junction. *Applied physics letters*, 94(16):164107–164107, 2009.

[16] Amit Gupta and Ranganathan Kumar. Flow regime transition at high capillary numbers in a microfluidic t-junction: viscosity contrast and geometry effect. *Physics of Fluids*, 22:122001, 2010.

[17] Amit Gupta and Ranganathan Kumar. Effect of geometry on droplet formation in the squeezing regime in a microfluidic t-junction. *Microfluidics and Nanofluidics*, 8(6):799–812, 2010.

[18] T.M. Squires and S.R. Quake. Microfluidics: Fluid physics at the nanoliter scale. *Reviews of modern physics*, 77(3):977, 2005.

[19] H.A. Stone, A.D. Stroock, and A. Ajdari. Engineering flows in small devices. *Annu. Rev. Fluid Mech.*, 36:381–411, 2004.

[20] J. Voldman, M.L. Gray, and M.A. Schmidt. Microfabrication in biology and medicine. *Annual review of biomedical engineering*, 1(1):401–425, 1999.

[21] KK Jain. Applications of biochip and microarray systems in pharmacogenomics. *Pharmacogenomics*, 1(3):289–307, 2000.

[22] D.J. Beebe, G.A. Mensing, and G.M. Walker. Physics and applications of microfluidics in biology. *Annual review of biomedical engineering*, 4(1):261–286, 2002.

[23] P.J.A. Kenis, R.F. Ismagilov, and G.M. Whitesides. Microfabrication inside capillaries using multiphase laminar flow patterning. *Science*, 285(5424):83–85, 1999.

[24] J.L. Steinbacher and D.T. McQuade. Polymer chemistry in flow: New polymers, beads, capsules, and fibers. *Journal of Polymer Science Part A: Polymer Chemistry*, 44(22):6505–6533, 2006.

[25] S. Sugiura, M. Nakajima, J. Tong, H. Nabetani, and M. Seki. Preparation of monodispersed solid lipid microspheres using a microchannel emulsification technique. *Journal of colloid and interface science*, 227(1):95–103, 2000.

[26] W. Jeong, J. Kim, S. Kim, S. Lee, G. Mensing, and D.J. Beebe. Hydrodynamic microfabrication via on the fly photopolymerization of microscale fibers and tubes. *Lab Chip*, 4(6):576–580, 2004.

[27] S.E. Barnes, Z.T. Cygan, J.K. Yates, K.L. Beers, and E.J. Amis. Raman spectroscopic monitoring of droplet polymerization in a microfluidic device. *Analyst*, 131(9):1027–1033, 2006.

[28] Z. Nie, W. Li, M. Seo, S. Xu, and E. Kumacheva. Janus and ternary particles generated by microfluidic synthesis: design, synthesis, and self-assembly. *Journal of the American Chemical Society*, 128(29):9408–9412, 2006.

[29] Z. Nie, S. Xu, M. Seo, P.C. Lewis, and E. Kumacheva. Polymer particles with various shapes and morphologies produced in continuous microfluidic reactors. *Journal of the American Chemical Society*, 127(22):8058–8063, 2005.

[30] J.W. Kim, A.S. Utada, A. Fernández-Nieves, Z. Hu, and D.A. Weitz. Fabrication of monodisperse gel shells and functional microgels in microfluidic devices. *Angewandte Chemie*, 119(11):1851–1854, 2007.

[31] E. Quevedo, J. Steinbacher, and D.T. McQuade. Interfacial polymerization within a simplified microfluidic device: capturing capsules. *Journal of the American Chemical Society*, 127(30):10498–10499, 2005.

[32] M. Seo, Z. Nie, S. Xu, M. Mok, P.C. Lewis, R. Graham, and E. Kumacheva. Continuous microfluidic reactors for polymer particles. *Langmuir*, 21(25):11614–11622, 2005.

[33] R.F. Shepherd, J.C. Conrad, S.K. Rhodes, R. Darren, M. Marquez, D.A. Weitz, and J.A. Lewis. Microfluidic assembly of homogeneous and janus colloid-filled hydrogel granules. *Langmuir*, 22(21):8618–8622, 2006.

[34] D. Dendukuri, K. Tsoi, T.A. Hatton, and P.S. Doyle. Controlled synthesis of nonspherical microparticles using microfluidics. *Langmuir*, 21(6):2113–2116, 2005.

[35] A. Kubo, H. Shinmori, and T. Takeuchi. Atrazine-imprinted microspheres prepared using a microfluidic device. *Chemistry Letters*, 35(6):588–589, 2006.

[36] T. Nisisako, T. Torii, and T. Higuchi. Novel microreactors for functional polymer beads. *Chemical Engineering Journal*, 101(1):23–29, 2004.

[37] T. Nisisako, T. Torii, T. Takahashi, and Y. Takizawa. Synthesis of monodisperse bicolored janus particles with electrical anisotropy using a microfluidic co-flow system. *Advanced Materials*, 18(9):1152–1156, 2006.

[38] S.H. Cho, J.B. Jun, J.H. Ryu, and K.D. Suh. Preparation of monodisperse poly (divinylbenzene) macrobeads via a drop breaking and polymerization method. *Colloids and Surfaces A: Physicochemical and Engineering Aspects*, 254(1):1–7, 2005.

[39] G.A. Groß, C. Hamann, PM Günther, and JM Köhler. Formation of polymer and nanoparticle doped polymer minirods by use of the microsegmented flow principle. *Chemical engineering & technology*, 30(3):341–346, 2007.

[40] Adam C Siegel, Derek A Bruzewicz, Douglas B Weibel, and George M Whitesides. Microsolidics: Fabrication of three-dimensional metallic microstructures in poly (dimethylsiloxane). *Advanced Materials*, 19(5):727–733, 2007.

[41] S. Hong, H.J. Hsu, R. Kaunas, and J. Kameoka. Collagen microsphere production on a chip. *Lab on a Chip*, 2012.

[42] Linyou Cao, David N Barsic, Alex R Guichard, and Mark L Brongersma. Plasmon-assisted local temperature control to pattern individual semiconductor nanowires and carbon nanotubes. *Nano letters*, 7(11):3523–3527, 2007.

[43] Caihong Fang, Lei Shao, Yihua Zhao, Jianfang Wang, and Hongkai Wu. A gold nanocrystal/poly (dimethylsiloxane) composite for plasmonic heating on microfluidic chips. *Advanced Materials*, 24(1):94–98, 2012.

[44] Y.J. Eun, A. Utada, M.F. Copeland, S. Takeuchi, and D.B. Weibel. Encapsulating bacteria in agarose microparticles using microfluidics for high-throughput cell analysis and isolation. *ACS chemical biology*, 6(3):260, 2011.

[45] W.M. Sigmund, N.S. Bell, and L. Bergström. Novel powder-processing methods for advanced ceramics. *Journal of the American Ceramic Society*, 83(7):1557–1574, 2000.

[46] J.H. Kim, W.C. Choi, H.Y. Kim, Y. Kang, and Y.K. Park. Preparation of mono-dispersed mixed metal oxide micro hollow spheres by homogeneous precipitation in a micro precipitator. *Powder technology*, 153(3):166–175, 2005.

[47] A. Fang, C. Gosse, C. Gaillard, X. Zhao, and J. Davy. Tuning silica particle shape at fluid interfaces. *Lab on a Chip*, 2012.

[48] L. Bergström and E. Sjöström. Temperature induced gelation of concentrated ceramic suspensions: rheological properties. *Journal of the European Ceramic Society*, 19(12):2117–2123, 1999.

[49] F.F. Lange. Powder processing science and technology for increased reliability. *Journal of the American Ceramic Society*, 72(1):3–15, 2005.

[50] LJ Gauckler, T. Graule, and F. Baader. Ceramic forming using enzyme catalyzed reactions. *Materials chemistry and physics*, 61(1):78–102, 1999.

[51] Y. Yang and WM Sigmund. Rheological properties and gelation threshold of temperature induced forming (tif) alumina suspensions with variation in molecular weight of polyacrylic acid. *Journal of Materials Synthesis and Processing*, 10(5):249–255, 2002.

[52] E. Yakhshi-Tafti, R. Kumar, and H.J. Cho. Measurement of surface interfacial tension as a function of temperature using pendant drop images. *International Journal of Optomechatronics*, 5(4):393–403, 2011.

[53] Yunfeng Lu, Hongyou Fan, Aaron Stump, Timothy L Ward, Thomas Rieker, and C Jeffrey Brinker. Aerosol-assisted self-assembly of mesostructured spherical nanoparticles. *Nature*, 398(6724):223–226, 1999.

[54] Y. Yang and W.M. Sigmund. A new approach to prepare highly loaded aqueous alumina suspensions with temperature sensitive rheological properties. *Journal of the European Ceramic Society*, 23(2):253–261, 2003.

[55] Y. Xia and G.M. Whitesides. Soft lithography. *Annual review of materials science*, 28(1):153–184, 1998.